ACS Energy LETTERS

http://pubs.acs.org/journal/aelccp

LETTER

Stress Engineering for Mitigating Thermal Cycling Fatigue in Perovskite Photovoltaics

Min Chen,*,# Yifan Dong,# Yi Zhang,# Xiaopeng Zheng,# Gabriel R. McAndrews, Zhenghong Dai, Qi Jiang, Shuai You, Tuo Liu, Steven P. Harvey, Kai Zhu, Vincent Oliveto, Alec Jackson, Robert Witteck, Lance M. Wheeler, Nitin P. Padture, Paul J. Dyson, Michael D. McGehee, Mohammad K. Nazeeruddin, Matthew C. Beard, and Joseph M. Luther*

Cite This: *ACS Energy Lett.* 2024, 9, 2582−2589

Read Online

ACCESS | Metrics & More | Article Recommendations | Supporting Information

ABSTRACT: **Mechanical residual stresses within multilayer thin-film device stacks become problematic during thermal changes because of differing thermal expansion and contraction of the various layers. Thin-film photovoltaic (PV) devices are a prime example where this is a concern during temperature fluctuations that occur over long deployment lifetimes. Here, we show control of the residual stress within halide perovskite thin-film device stacks by the use of an alkyl-ammonium additive. This additive approach reduces the residual stress and strain to near-zero at room temperature and prevents cracking and delamination during intense and rapid thermal cycling. We demonstrate this concept in both n-i-p (regular) and p-i-n (inverted) unencapsulated perovskite solar cells and mini-modules with both types of solar cells retaining over 80% of their initial power conversion efficiency (PCE) after 2500 thermal cycles in the temperature range of −40 to 85 °C. The mechanism by which stress engineering mitigates thermal cycling fatigue in these perovskite PVs is discussed.**

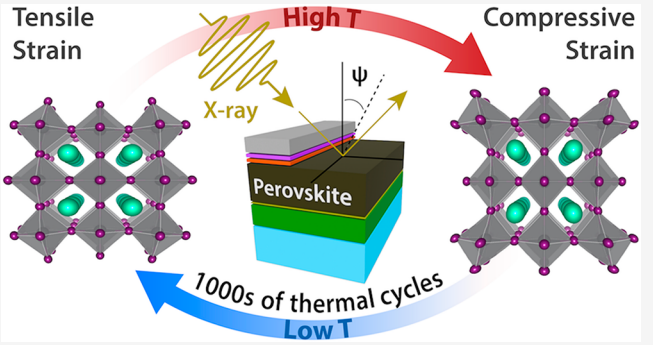

Halide perovskite semiconductors are a promising emerging photovoltaic (PV) technology, but to rapidly reach the commercialization stage, performance and upscaling must be achieved along with demonstrated reliability in operation and under conditions exceeding the testing conditions in which perovskites are routinely measured.[1−6] For commercialization, perovskite solar cells (PSCs) must undergo and pass rigorous testing protocols accepted by the research community, such as International Summit on Organic Photovoltaic Stability (ISOS) procedures.[7] PSCs are being explored for various applications, e.g., extraterrestrial environments,[8,9] and a primary challenge in this context is the ISOS-T-3 thermal cycling test, which simulates conditions ranging from −40 to 85 °C. Although the thermal stability of PSCs shows them to be capable of this, the reported lifetime n_{80} (number of thermal cycles performed while retaining at least 80% initial efficiency) is approximately 200−300 thermal cycles.[10−15] During thermal cycling, the decay of the mechanical integrity is the main cause of the performance degradation, which remains poorly understood.[11,12]

While significant improvements have been demonstrated in the stability and upscaling of these materials (large-area PSCs and perovskite modules), few reports have focused on their mechanical reliability.[16−20] PSCs have a low fracture energy within the perovskite materials themselves, and low interfacial adhesion energies in the layered PSC device stacks.[21−23] Appropriately matching the coefficient of thermal expansion of the perovskite layer to that of the adjoining layers prevents fracture and premature delamination but is challenging to accomplish given other constraints for high efficiency.[24,25] Several research efforts have been dedicated to improving the mechanical reliability. Dai et al. demonstrated that treatment with self-assembled monolayers that react with surface hydroxyl groups results in a 50% increase in the adhesion toughness between the electron transport layer (ETL) and perovskite layer.[17] Cheacharoen et al. also showed PSCs in an encapsulant (ethylene vinyl acetate) with a low elastic modulus

Received: April 9, 2024
Revised: April 29, 2024
Accepted: April 30, 2024
Published: May 8, 2024

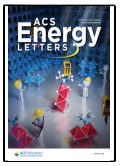

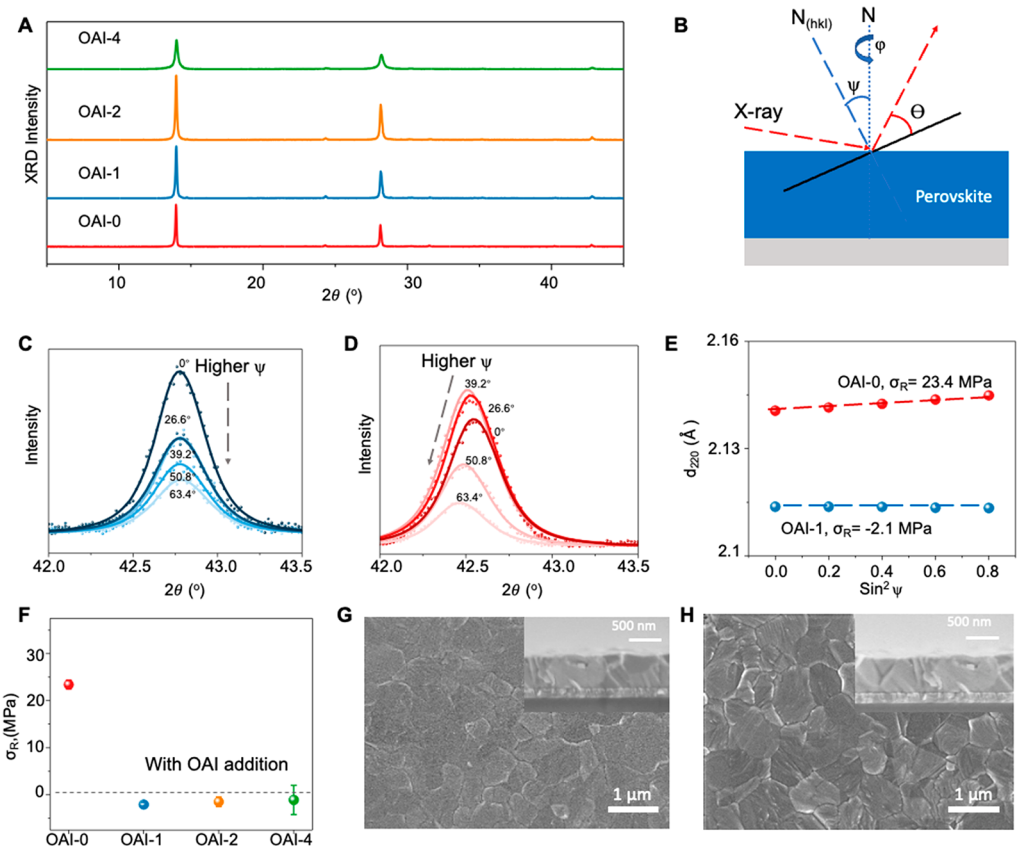

Figure 1. (A) XRD patterns of the perovskite thin films with molar ratios of 0, 1%, 2%, and 4% of OAI to Pb, which were designated as OAI-0, OAI-1, OAI-2, and OAI-4, respectively. (B) Schematic illustration of the XRD sin$^2\psi$ method for quantifying the residual stress. Note that the stress for the perovskite is measured in the n-i-p device stack. (C) XRD patterns at different tilt angles for the OAI-1 perovskite thin film. Higher values of ψ are shown as lighter colored lines. The specific angles ψ chosen for strain analysis are shown in Figure 1C,D (0°, 26.6°, 39.2°, 50.8°, and 63.4°). (D) XRD pattern at different tilt angles for the OAI-0 perovskite thin films. Higher values of ψ are shown in progressively lighter colored lines. (E) d_{220} spacing versus sin$^2\psi$ for the OAI-0 and OAI-1 perovskite thin films. (F) Comparison of the residual stress in the OAI-0, OAI-1, OAI-2, and OAI-4 perovskite thin films. Top-view SEM images of (G) OAI-0 and (H) OAI-1 perovskite thin films (inset, cross-sectional SEM image of the corresponding perovskite thin film).

to enable mechanical reliability that retained more than 90% of their initial performance after 200 thermal cycles.[11] However, less attention has been given to the perovskite thin film layers, which are sensitive and vital for improving the mechanical reliability and PV performance.

In this study, we demonstrate control over the residual stress of perovskite thin films after thermal annealing by incorporating alkyl ammonium molecules, such as *n*-octylammonium iodide (OAI), into the perovskite precursor and, thus, thin films. Because of the relatively large size of the OA^+ cation, we and others believe that these ammonium molecules mainly incorporate at grain boundaries and interfaces rather than internally within the perovskite lattice during crystallization[26,27] and relieve internal stress (from ~23.4 to ~0 MPa) at room temperature (RT). This additive not only results in increased PCE for both p-i-n and n-i-p PSCs and unencapsulated perovskite solar minimodules (PSMs) but also, more importantly, improves the thermal cycling lifetime n_{80} to up to 500 thermal cycles in accordance with the ISOS-T-3 procedure and 2500 cycles in an accelerated thermal cycling test. The thermal cycling performance of PSCs and PSMs reveals that minimizing the residual stresses at RT in perovskite thin films reduces the residual stresses across the temperature range and prevents further interface delamination in layered PV devices during thermal cycling tests.

In the n-i-p geometry, which we will discuss first, the mixed-composition metal halide perovskite (MHP), $(FAPbI_3)_{0.95}(MAPbBr_3)_{0.05}$, was used for its high PCE and thermal stability, and SnO_2 was chosen for the ETL since it offers more favorable energy level alignment with MHP and less possible photocatalytic degradation with MHP compared with TiO_2.[28] We explored a series of alkylammonium halides but focused specifically on *n*-octylammonium iodide with an alkyl $(CH_2)_n$ (n = 8) linker, which appears to best reduce the residual internal stress in perovskite thin films. Additionally, we varied the concentration by dissolving different amounts (0, 1%, 2%, and 4%) of OAI in the perovskite precursor solution before spin coating and created a set of perovskite thin films with 0, 1%, 2%, and 4% of OAI designated as OAI-0, OAI-1, OAI-2, and OAI-4, respectively. Figure 1A shows the XRD results for the set of perovskite films prepared following spin coating and thermal annealing at 100 °C for 40 min. A decrease in the XRD intensity of the OAI-4 peak is observed, while the XRD intensities of the (001) and (002) peaks of OAI-1 and OAI-2 remain mostly unchanged. The high concentration of OAI in OAI-4 disrupts crystallization, which results in the lower XRD intensity, as shown in Figure 1A, and slightly lower domain size, as presented in Table S2. Previous literature has reported that alkylammonium molecules can be found at grain boundaries of the perovskite thin films after annealing,[29−33]

https://doi.org/10.1021/acsenergylett.4c00988
ACS Energy Lett. 2024, 9, 2582−2589

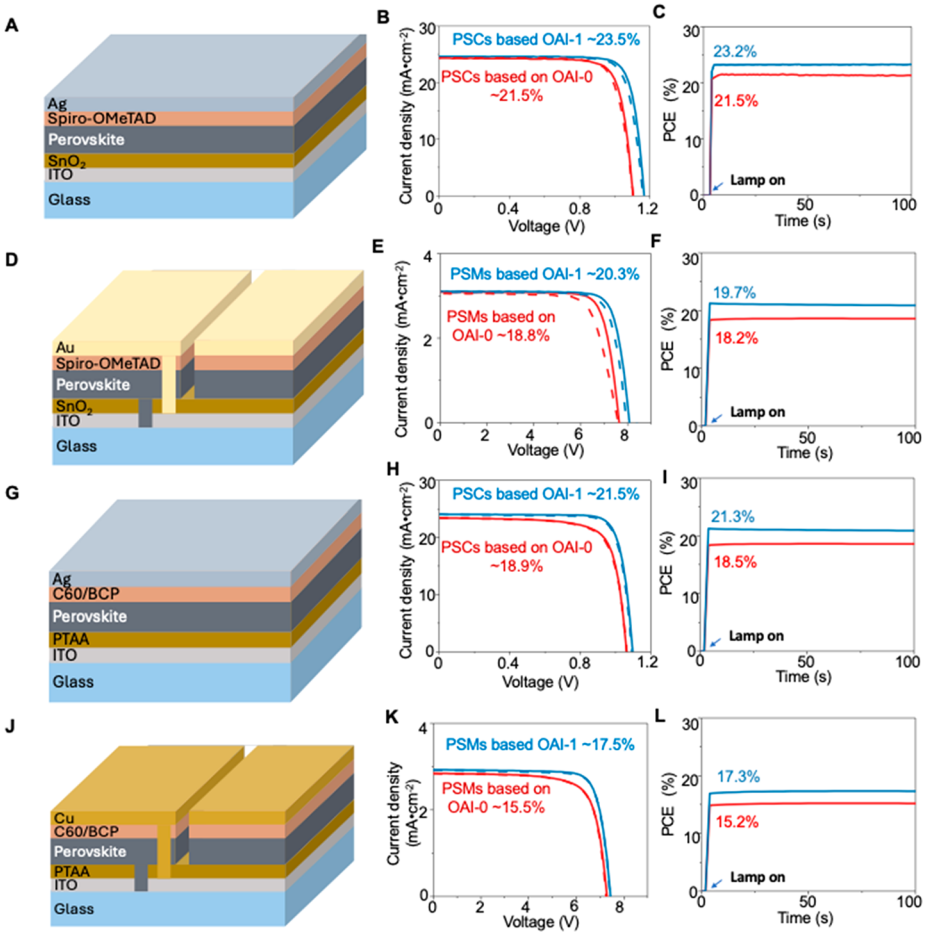

Figure 2. (A–D) Schematic illustration (not to scale) of the n-i-p regular planar PSCs. (B) *J–V* responses, in reverse and forward scans, of champion n-i-p PSCs based on OAI-0 and OAI-1 perovskite thin films. (C) Stable output of champion n-i-p PSCs measured at a constant voltage. (D) Schematic illustration (not to scale) of the n-i-p regular planar PSMs. (E) *J–V* responses, in reverse and forward scans, of champion n-i-p PSMs based on OAI-0 and OAI-1 perovskite thin films. (F) Stable output of champion n-i-p PSMs measured at constant voltage. (G) Schematic illustration (not to scale) of the p-i-n inverse planar PSCs. (H) *J–V* responses, in reverse and forward scans, of champion p-i-n PSCs based on OAI-0 and OAI-1 perovskite thin films. (I) Stable output of champion p-i-n PSCs measured at constant voltage. (J) Schematic illustration (not to scale) of the unencapsulated p-i-n inverse planar perovskite solar minimodules (PSMs). (K) *J–V* responses, in reverse and forward scans, of champion p-i-n PSMs based on OAI-0 and OAI-1 perovskite thin films. (L) Stable output of champion p-i-n PSMs measured at constant voltage.

and we agree with that assessment. We used time-of-flight secondary ion mass spectrometry (ToF-SIMS) to track the specific mass signature of the alkyl molecule. The corresponding ToF-SIMS maps are included in Figure S1, which show a uniform spatial distribution in the OAI-1 and OAI-4 perovskite films. Given the homogeneous distribution and that we do not see a change in the XRD pattern that would occur if OA^+ occupied an A-site, we conclude it is likely that the alkyl molecules are between grains and/or at grain surfaces.[29−33]

The XRD $\sin^2\psi$ method (scheme illustrated in Figure 1B) is a sensitive method for probing the residual internal stress/strain in perovskite thin films with different amounts of OAI.[34] The perovskite films were deposited on glass/indium tin oxide (ITO)/SnO_2 to resemble those used in devices following the method of Jiang et al.[35] In Figure 1C,D, the (220) interplanar spacing (d_{220}) is plotted as a function of $\sin^2\psi$ for OAI-0 and OAI-1, respectively. The monotonic decrease in the intensity of diffraction peaks as a function of ψ for the OAI-1 (Figure 1C) is possibly caused by a decrease in penetration depth. However, for OAI-0 (Figure 1D), the intensity is higher for ψ = 26.6° and ψ = 39.2°, which suggests a different distribution of crystallite orientation compared with OAI-1.[36] In other words, for OAI-0, there is an increased population of crystallites oriented at ψ = 26.6° and ψ = 39.2°.

The positive slope (m) of the linear fit to the d_{220}-$\sin^2\psi$ data for the axially aligned phase of OAI-0 indicates the presence of residual biaxial tensile residual stress (or strain). In contrast, OAI-1 shows a much lower magnitude and negative slope, which suggests they likely transition to very weak residual compressive strain, which we term as near zero in comparison with the initial compressive case. The biaxial residual stress can be calculated using the equation

$$\sigma_R = \left(\frac{E_{\langle 220\rangle}}{1+\nu}\right)\left(\frac{m}{d_n}\right)$$

where m is the slope of the linear fit to the data, d_n is the d_{220} spacing at $\sin^2\psi = 0$ (y intercept), $E_{\langle 220\rangle}$ is Young's modulus in the ⟨220⟩ direction, and ν is Poisson's ratio. $E_{\langle 220\rangle}$ is estimated to be 12 GPa.[22,37] A typical ν value of 0.33 is assumed.[38] The calculated residual internal stresses for the set of perovskite thin films are summarized in Figure 1F. Overall, the tensile

https://doi.org/10.1021/acsenergylett.4c00988
ACS Energy Lett. 2024, 9, 2582−2589

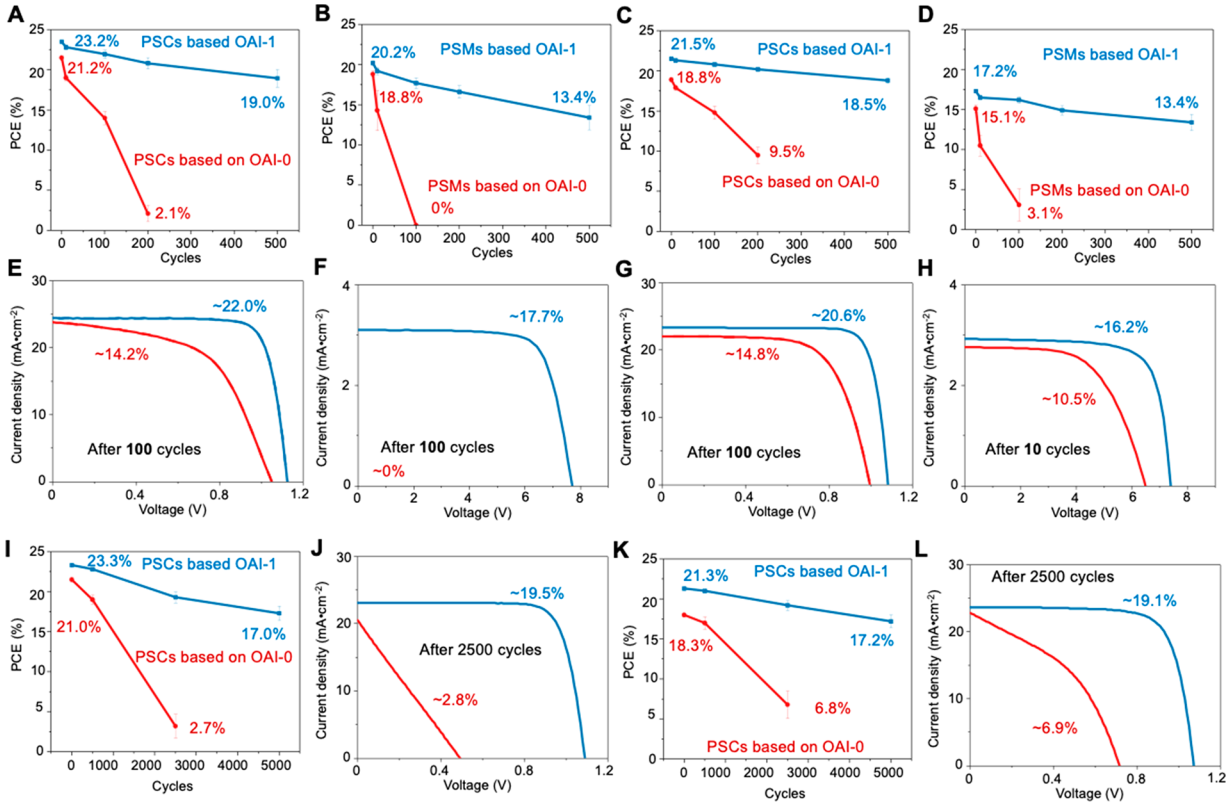

Figure 3. Evolution of the PCE of n-i-p PSCs (A), n-i-p PSMs (B), p-i-n PSCs (C), and p-i-n PSMs (D) over 500 temperature cycles between −40 and 85 °C, 6 h per cycle. Typical *J*−*V* curves (reverse scan) were obtained after 100 cycles for the n-i-p PSCs (E), n-i-p PSMs (F), and p-i-n PSCs (G) and after 10 cycles of the p-i-n PSMs (H). The evolution of the PCE of n-i-p PSCs (I) and p-i-n PSCs (K) over 5000 temperature cycles between −40 and 85 °C for 5 min per cycle. Typical *J*−*V* curves (reverse scan) after 2500 cycles were obtained for the n-i-p PSCs (J) and p-i-n PSCs (L).

stress in OAI-0 is calculated to be 23.4 MPa, which is reduced to nearly 0 MPa in OAI-1, OAI-2, and OAI-4 (showing minor compressive strain). On the basis of this, the OAI-0 and OAI-1 samples were chosen for further morphological characterization using scanning electron microscopy (SEM). Figure 1G,H shows that the average apparent grain sizes of OAI-0 and OAI-1 are approximately 810 and 820 nm, respectively. Williamson−Hall (WH) analysis was performed to identify the influence of OAI on structural or compositional inhomogeneity, as well as verify the comparable grain sizes from SEM. The results of WH analysis are summarized in Figure S2 and Table S2 and, within measurement uncertainty, show the addition of OAI has minimal impact on the microstrain and grain size.

To examine the PV performance, PSCs based on OAI-0 and OAI-1 were then prepared in both planar n-i-p and p-i-n device structures. Figure 2A shows the n-i-p structure comprising glass/ITO/SnO_2/perovskite/Spiro-OMeTAD/Ag, and Figure 2G shows the p-i-n device structure comprising glass/ITO/poly[bis(4-phenyl)(2,4,6-trimethylphenyl)amine] (PTAA)/perovskite/C_{60}/bathocuproine (BCP)/Ag. The composition of the perovskite is the same in both cases. The current density (J)−voltage (V) response under AM1.5G of the best performing n-i-p and p-i-n PSCs based on OAI-0 and OAI-1 are presented in Figure 2B,H, and the corresponding PV performance parameters are listed in Table S1. The addition of OAI increased the open-circuit voltage (V_{OC}) from 1.11 to 1.17 V in the n-i-p device and from 1.06 to 1.09 V in the p-i-n device with little hysteresis. The short-circuit current density (J_{SC}) values for the best PSC based on OAI-1 compared favorably with the respective values derived from the external quantum efficiency (EQE) spectra of the PSC based on OAI-1 in Figure S3. The stabilized power output at the maximum power point (MPP) of these PSCs is presented in Figure 2C,F as the PCE. Statistics for the PV performance parameters J_{SC}, V_{OC}, fill factor (FF), and PCE for PSCs (20 cells of each type) are presented in Figure S4 and demonstrate reproducibility. We also prepared both n-i-p and p-i-n perovskite solar minimodules (PSMs) on the basis of OAI-0 and OAI-1. The J−V responses of the best performing n-i-p and p-i-n PSMs are shown in Figure 2E,K with values of 20.3% for the n-i-p PSM and 17.5% for the p-i-n PSM, and the corresponding PV performance parameters are listed in Table S2.

All PSCs and PSMs based on OAI-0 and OAI-1 were put into a closed chamber (shown in Figure S5) for thermal cycling under the recommendations provided by the ISOS-T-3 procedure (−40 to 85 °C, N_2, 6 h per cycle). For the n-i-p PSCs and PSMs, the PCE of the PSCs based on OAI-0 decreased quickly from the initial 21.2% value to 2.1% after 200 cycles, while the PCE of the PSCs based on OAI-1 retained 19.0% (82% of the initial PCE of 23.2%). However, we observed a much faster degradation in n-i-p PSMs without the OAI additive (OAI-0), which decreased to 0% after 100 cycles. The PCE of the n-i-p PSM based on OAI-1 decreased to 17.7% after 100 cycles and 13.4% after 500 cycles. For p-i-n PSCs and PSMs, the PCE of PSCs based on OAI-0 decreased from 18.5% to 9.5% after 200 cycles, while the PCE of PSCs based on OAI-1 decreased to 20.2% (94% of the initial PCE).

https://doi.org/10.1021/acsenergylett.4c00988
ACS Energy Lett. 2024, 9, 2582−2589

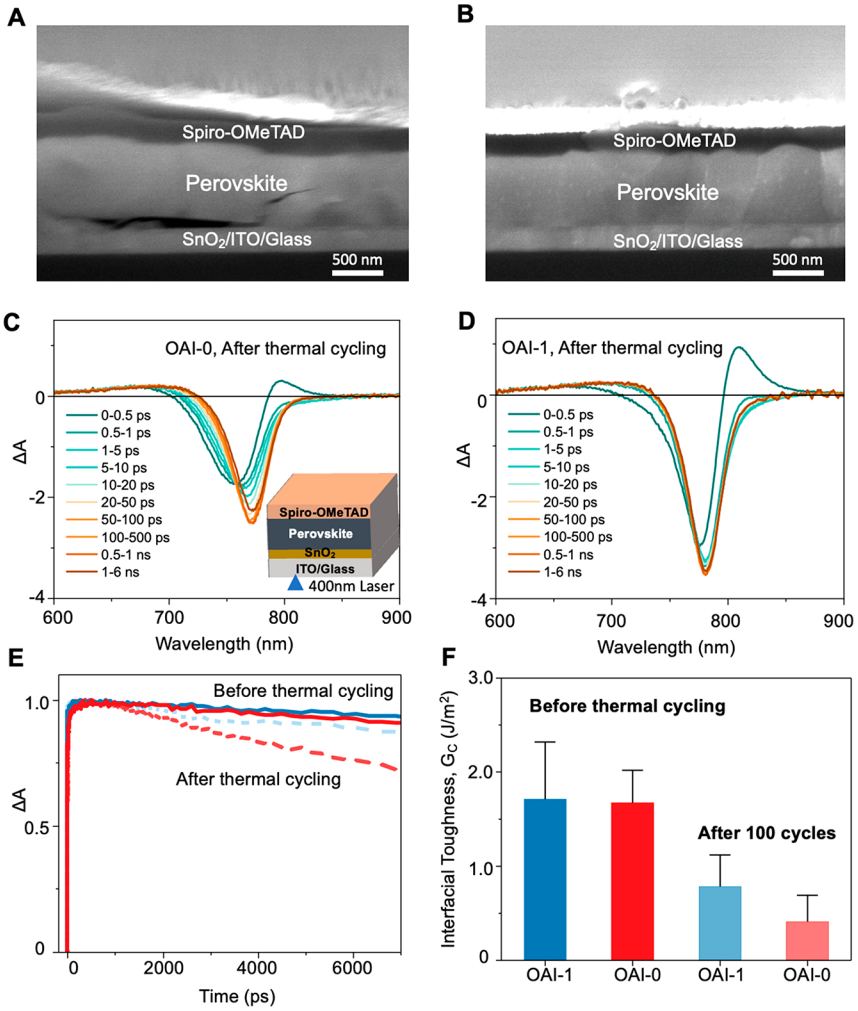

Figure 4. Cross-sectional SEM images of the as-fabricated PSCs (A) with OAI-0 and (B) with OAI-1 after thermal cycling. TA spectra at various pump-probe delay times of the PSCs (C) with OAI-0 and (D) with OAI-1 after thermal cycling. The pump excitation energy is 3.1 eV (400 nm) at the SnO_2/perovskite interface. (E) TA kinetics summary for PSCs (C) with OAI-0 and (D) with OAI-1 after thermal cycling. Solid line: before thermal cycling. Dotted line: after thermal cycling. (F) Interfacial toughness of SnO_2/perovskite thin films in solar cell structures calculated using the double cantilever beam method before and after thermal cycling.

The $J-V$ curves for PSCs and PSMs after 100 cycles are shown in Figure 2B,D,F, and after 10 cycles in Figure 2H, with the main loss ocurring in the FF and V_{OC}. Both n-i-p and p-i-n PSCs demonstrated a critical point (100 cycles for n-i-p PSCs and p-i-n PSCs) where they transition from slower decay to faster decay.

We also tested n-i-p and p-i-n PSCs in an accelerated thermal cycling test capable of a much greater total number of cycles in a reasonable amount of time (see the Supporting Information for more details). The thermal shock test was set as −40 to 85 °C with 5 min per cycle, which may represent harsher cycling conditions for PSCs with faster ΔT and a greater number of total cycles. The n-i-p and p-i-n PSCs based on OAI-1 still maintain 72% and 81% of the initial efficiency after 5000 cycles, respectively, while the n-i-p and p-i-n PSCs based on OAI-0 only retain 13% and 37%, respectively, after 2500 cycles. To the best of our knowledge, this is the first report of thermal cycle testing exceeding 500 cycles. From the $J-V$ response of the n-i-p (Figure 3J) and p-i-n (Figure 3L) PSCs based on the OAI-1 and OAI-0, the main loss of PV performance during rapid thermal cycling is also the reduction in V_{OC} and FF, which is consistent with the observation of PCE evolution during standard thermal cycling. Furthermore, in p-i-n PSCs, we modified the perovskite composition and improved the PCE of p-i-n solar cells based on the OAI-1 to 24.3%. The improved p-i-n solar cells based on OAI-1 are more resistant to degradation than the improved p-i-n cells based on OAI-0 in thermal cycling test (Figure S6). To better understand this behavior, we comprehensively characterized the n-i-p PSCs after 100 cycles, and the results are presented below.

Cross-sectional SEM images of the PSC based on OAI-0 after 100 cycles (Figure 4A) revealed two types of irreversible morphological degradation features at the interface: cracks in the grains and delamination at the interface between the perovskite and SnO_2 layers. In contrast, such degradation features were not observed in the corresponding SEM image of the PSC based on OAI-1 (Figure 4B). We also performed XRD for PSCs based on OAI-0 and OAI-1 after different numbers of thermal cycles, as shown in Figure S7. The XRD pattern shows a lack of an obvious 2D phase (which would be apparent at angles less than 10°) formed during the perovskite deposition process.[30] Before 100 cycles were reached, no additional XRD peaks corresponding to the PSCs were

https://doi.org/10.1021/acsenergylett.4c00988
ACS Energy Lett. 2024, 9, 2582−2589

observed, and only a small decrease (~5%) in the XRD peak intensity could be observed for the perovskite layer. However, after 100 cycles, a decrease in the intensity (~35% drop) was observed in the PSCs based on OAI-0, which indicates accelerated structural disorder of the perovskite materials after delamination, similar to what is commonly reported for flexible solar cells.[16,39]

Moreover, the PSCs based on OAI-0 and OAI-1 before (Figure S8) and after 100 cycles of thermal cycling were also examined by transient absorption (TA) spectroscopy. A laser with a wavelength of 400 nm was used to illuminate the glass side so that the TA signal was predominantly generated from the interface of the perovskite and SnO_2 layers, thereby enabling us to probe the behavior of the photocarriers generated from the interface of the perovskite and SnO_2 layers before and after thermal cycling. We also deposited pure OAI-0 and OAI-1 onto glass/ITO substrates for comparison. After 100 thermal cycles, the TA kinetics results (Figure S9) show negligible differences between OAI-0 and OAI-1. However, after 100 cycles of thermal cycling, compared with the TA kinetics results for pure OAI-0 and OAI-1, we clearly observed a shorter lifetime in PSCs based on the OAI-0, which we believe is a single-layer passivation from the hole transport layer (HTL)/perovskite interface because of the delamination between the perovskite layer and the ETL, as shown by SEM (Figure 4A). The delamination effect between the perovskite thin films and the ETL layer before and after thermal cycling was also examined by measuring the interfacial toughness (G_C) between the perovskite thin films and the ETL layer using a dual beam cantilever technique (Figure 4F). The G_C value before thermal cycling shows negligible differences for the PSCs based on the OAI-0 (1.67 ± 0.32 J/m^2) and the OAI-1 (1.71 ± 0.45 J/m^2). After 100 thermal cycles, the G_C value inevitably decreases to 0.41 ± 0.25 for PSCs based on OAI-0 and 0.78 ± 0.22 J/m^2 for those based on OAI-1 (Figure 4F). The fractured surfaces (before and after thermal cycling) are presented in Figure S10, which indicates the beneficial effect of the OAI in preserving the mechanical integrity of the buried interface during thermal cycling. For the PSCs based on the OAI-1, the neutral residual stress of the OAI-1 at room temperature allows the perovskite layer to better match the adjacent layers and endure the changes that result from temperature fluctuations. Furthermore, the grain surfaces benefit from the OAI molecules, which could help isolate grains from increasing stress, which in turn prevents mechanical failure. However, without the additive, the high residual tensile stress in the OAI-0 PSCs facilitates a decrease in the interfacial toughness after thermal cycling and leads to fatigue.[40,41] Taken together, our results suggest that stress engineering of perovskite thin films in PSCs or PSMs is an effective approach for significantly enhancing the thermal cycling performance of perovskite PV devices, as demonstrated by using multiple common device structures.

■ ASSOCIATED CONTENT

Data Availability Statement

All data are available in the main text or the Supporting Information.

Supporting Information

The Supporting Information is available free of charge at https://pubs.acs.org/doi/10.1021/acsenergylett.4c00988.

Details on materials and methods, including device fabrication, materials characterization, mechanical testing, device characterization, supporting Figures S1−S9, Tables S1 and S2, and additional supporting references (PDF)

■ AUTHOR INFORMATION

Corresponding Authors

Min Chen − *National Renewable Energy Laboratory, Golden, Colorado 80401, United States*; Email: min.chen@nrel.gov

Joseph M. Luther − *National Renewable Energy Laboratory, Golden, Colorado 80401, United States*; orcid.org/0000-0002-4054-8244; Email: joey.luther@nrel.gov

Authors

Yifan Dong − *National Renewable Energy Laboratory, Golden, Colorado 80401, United States*; orcid.org/0000-0003-2912-3322

Yi Zhang − *Institute of Chemical Sciences and Engineering, École Polytechnique Fedérale de Lausanne (EPFL), 1015 Lausanne, Switzerland*; orcid.org/0000-0001-5710-3404

Xiaopeng Zheng − *National Renewable Energy Laboratory, Golden, Colorado 80401, United States*

Gabriel R. McAndrews − *Materials Science and Engineering Program, University of Colorado Boulder, Boulder, Colorado 80303, United States*

Zhenghong Dai − *School of Engineering, Brown University, Providence, Rhode Island 02912, United States*

Qi Jiang − *National Renewable Energy Laboratory, Golden, Colorado 80401, United States*; orcid.org/0000-0001-7122-3664

Shuai You − *National Renewable Energy Laboratory, Golden, Colorado 80401, United States*

Tuo Liu − *National Renewable Energy Laboratory, Golden, Colorado 80401, United States*; orcid.org/0000-0003-4405-0678

Steven P. Harvey − *National Renewable Energy Laboratory, Golden, Colorado 80401, United States*; orcid.org/0000-0001-6120-7062

Kai Zhu − *National Renewable Energy Laboratory, Golden, Colorado 80401, United States*; orcid.org/0000-0003-0908-3909

Vincent Oliveto − *Air Force Research Laboratory, Kirtland AFB, New Mexico 87117, United States*

Alec Jackson − *Air Force Research Laboratory, Kirtland AFB, New Mexico 87117, United States*

Robert Witteck − *National Renewable Energy Laboratory, Golden, Colorado 80401, United States*

Lance M. Wheeler − *National Renewable Energy Laboratory, Golden, Colorado 80401, United States*; orcid.org/0000-0002-1685-8242

Nitin P. Padture − *School of Engineering, Brown University, Providence, Rhode Island 02912, United States*; orcid.org/0000-0001-6622-8559

Paul J. Dyson − *Institute of Chemical Sciences and Engineering, École Polytechnique Fedérale de Lausanne (EPFL), 1015 Lausanne, Switzerland*; orcid.org/0000-0003-3117-3249

Michael D. McGehee − *Materials Science and Engineering Program, University of Colorado Boulder, Boulder, Colorado 80303, United States*; orcid.org/0000-0001-9609-9030

Mohammad K. Nazeeruddin − *Institute of Chemical Sciences and Engineering, École Polytechnique Fedérale de Lausanne*

https://doi.org/10.1021/acsenergylett.4c00988
ACS Energy Lett. 2024, 9, 2582−2589

(EPFL), 1015 Lausanne, Switzerland; orcid.org/0000-0001-5955-4786

Matthew C. Beard − *National Renewable Energy Laboratory, Golden, Colorado 80401, United States;* orcid.org/0000-0002-2711-1355

Complete contact information is available at: https://pubs.acs.org/10.1021/acsenergylett.4c00988

Author Contributions

M.C. and J.M.L. conceived, designed, and supervised the research. M.C., Y.Z., and X.Z. fabricated the thin films and devices. Y.D. and M.C.B. performed and analyzed the optical characterization. G.R.M., Q.J., S.Y., and T.L. characterized and tested the XRD patterns of the thin films and devices. S.P.H. performed the TOF-SIMS characterization and analysis. Z.D. and N.P.P. performed the interfacial toughness tests and calculations. V.O. and A.J. conducted the rapid thermal cycling. All other authors contributed to the discussion of the mechanical behavior and PV performance during the thermal cycling test. L.M.W. also created the TOC graphic. M.C. and J.M.L. interpreted the data and drafted the manuscript, with contributions from the other authors.

Author Contributions

#M.C., Y.D., Y.Z., and X.Z. authors contributed equally.

Notes

The authors declare the following competing financial interest(s): M.D.M. is an advisor to Swift Solar.

■ ACKNOWLEDGMENTS

This work was authored in part by the National Renewable Energy Laboratory, operated by the Alliance for Sustainable Energy, LLC, for the U.S. Department of Energy (DOE) under Contract No. DE-AC36-08GO28308. The device fabrication and thermal cycling work was supported by the Operational Energy Capability Improvement Fund (OECIF) of the U.S. Department of Defense (DOD). Spectroscopy measurements were supported by the Center for Hybrid Organic Inorganic Semiconductors for Energy (CHOISE), an Energy Frontier Research Center funded by the Office of Basic Energy Sciences, Office of Science, within the US Department of Energy. G.R.M. and M.D.M. were supported by the Office of Naval Research (ONR) under award number N00014-20-1-2573. Z.D. and N.P.P. acknowledge the support from ONR (award no. N00014-20-1-2574). The views expressed in the article do not necessarily represent the views of the DOE or the U.S. Government.

■ REFERENCES

(1) Kojima, A.; Teshima, K.; Shirai, Y.; Miyasaka, T. Organometal Halide Perovskites as Visible-Light Sensitizers for Photovoltaic Cells. *J. Am. Chem. Soc.* **2009**, *131*, 6050−6051.

(2) Jena, A. K.; Kulkarni, A.; Miyasaka, T. Halide Perovskite Photovoltaics: Background, Status, and Future Prospects. *Chem. Rev.* **2019**, *119*, 3036−3103.

(3) Park, N.-G.; Grätzel, M.; Miyasaka, T.; Zhu, K.; Emery, K. Towards stable and commercially available perovskite solar cells. *Nature Energy* **2016**, *1*, 16152.

(4) Fei, C.; et al. Lead-chelating hole-transport layers for efficient and stable perovskite minimodules. *Science* **2023**, *380*, 823−829.

(5) Mei, A.; et al. Stabilizing Perovskite Solar Cells to IEC61215:2016 Standards with over 9,000-h Operational Tracking. *Joule* **2020**, *4*, 2646−2660.

(6) Bu, T.; et al. Modulating crystal growth of formamidinium−caesium perovskites for over 200 cm2 photovoltaic sub-modules. *Nature Energy* **2022**, *7*, 528−536.

(7) Khenkin, M. V.; et al. Consensus statement for stability assessment and reporting for perovskite photovoltaics based on ISOS procedures. *Nature Energy* **2020**, *5*, 35−49.

(8) Kirmani, A. R.; et al. Metal oxide barrier layers for terrestrial and space perovskite photovoltaics. *Nature Energy* **2023**, *8*, 191−202.

(9) Delmas, W.; et al. Evaluation of Hybrid Perovskite Prototypes After 10-Month Space Flight on the International Space Station. *Adv. Energy Mater.* **2023**, *13*, 2203920.

(10) Li, G.; et al. Highly efficient p-i-n perovskite solar cells that endure temperature variations. *Science* **2023**, *379*, 399−403.

(11) Cheacharoen, R.; et al. Encapsulating perovskite solar cells to withstand damp heat and thermal cycling. *Sustainable Energy & Fuels* **2018**, *2*, 2398−2406.

(12) Cheacharoen, R.; et al. Design and understanding of encapsulated perovskite solar cells to withstand temperature cycling. *Energy Environ. Sci.* **2018**, *11*, 144−150.

(13) He, J.; et al. Influence of phase transition on stability of perovskite solar cells under thermal cycling conditions. *Sol. Energy* **2019**, *188*, 312−317.

(14) Sheikh, A. D.; et al. Effects of High Temperature and Thermal Cycling on the Performance of Perovskite Solar Cells: Acceleration of Charge Recombination and Deterioration of Charge Extraction. *ACS Appl. Mater. Interfaces* **2017**, *9*, 35018−35029.

(15) Kim, Y. C.; et al. Engineering interface structures between lead halide perovskite and copper phthalocyanine for efficient and stable perovskite solar cells. *Energy Environ. Sci.* **2017**, *10*, 2109−2116.

(16) Dong, Q.; et al. Flexible perovskite solar cells with simultaneously improved efficiency, operational stability, and mechanical reliability. *Joule* **2021**, *5*, 1587−1601.

(17) Dai, Z.; et al. Interfacial toughening with self-assembled monolayers enhances perovskite solar cell reliability. *Science* **2021**, *372*, 618−622.

(18) Holzhey, P.; Saliba, M. A full overview of international standards assessing the long-term stability of perovskite solar cells. *Journal of Materials Chemistry A* **2018**, *6*, 21794−21808.

(19) Li, G.; et al. Structure and Performance Evolution of Perovskite Solar Cells under Extreme Temperatures. *Adv. Energy Mater.* **2022**, *12*, 2202887.

(20) Schwenzer, J. A.; et al. Temperature Variation-Induced Performance Decline of Perovskite Solar Cells. *ACS Appl. Mater. Interfaces* **2018**, *10*, 16390−16399.

(21) Dong, Q.; et al. Interpenetrating interfaces for efficient perovskite solar cells with high operational stability and mechanical robustness. *Nat. Commun.* **2021**, *12*, 973.

(22) Dai, Z.; et al. The mechanical behavior of metal-halide perovskites: Elasticity, plasticity, fracture, and creep. *Scripta Materialia* **2023**, *223*, 115064.

(23) Yuan, G.; et al. Inhibited Crack Development by Compressive Strain in Perovskite Solar Cells with Improved Mechanical Stability. *Adv. Mater.* **2023**, *35*, 2211257.

(24) Dai, Z.; et al. Dual-Interface-Reinforced Flexible Perovskite Solar Cells for Enhanced Performance and Mechanical Reliability. *Adv. Mater.* **2022**, *34*, 2205301.

(25) Wang, H.; et al. Interfacial Residual Stress Relaxation in Perovskite Solar Cells with Improved Stability. *Adv. Mater.* **2019**, *31*, 1904408.

(26) Lee, J.-W.; Tan, S.; Seok, S. I.; Yang, Y.; Park, N.-G. Rethinking the A cation in halide perovskites. *Science* **2022**, *375*, No. eabj1186.

(27) Zheng, X.; et al. Managing grains and interfaces via ligand anchoring enables 22.3%-efficiency inverted perovskite solar cells. *Nature Energy* **2020**, *5*, 131−140.

(28) Min, H.; et al. Perovskite solar cells with atomically coherent interlayers on SnO2 electrodes. *Nature* **2021**, *598*, 444−450.

(29) Chen, M.; et al. High-Performance Lead-Free Solar Cells Based on Tin-Halide Perovskite Thin Films Functionalized by a Divalent Organic Cation. *ACS Energy Letters* **2020**, *5*, 2223−2230.

(30) Alharbi, E. A.; et al. Cooperative passivation of perovskite solar cells by alkyldimethylammonium halide amphiphiles. *Joule* **2023**, *7*, 183−200.
(31) Gharibzadeh, S.; et al. Two birds with one stone: dual grain-boundary and interface passivation enables > 22% efficient inverted methylammonium-free perovskite solar cells. *Energy Environ. Sci.* **2021**, *14*, 5875−5893.
(32) Muscarella, L. A.; et al. Air-Stable and Oriented Mixed Lead Halide Perovskite (FA/MA) by the One-Step Deposition Method Using Zinc Iodide and an Alkylammonium Additive. *ACS Appl. Mater. Interfaces* **2019**, *11*, 17555−17562.
(33) Smock, S. R.; Chen, Y.; Rossini, A. J.; Brutchey, R. L. The Surface Chemistry and Structure of Colloidal Lead Halide Perovskite Nanocrystals. *Acc. Chem. Res.* **2021**, *54*, 707−718.
(34) McAndrews, G. R.; Guo, B.; Morales, D. A.; Amassian, A.; McGehee, M. D. How the dynamics of attachment to the substrate influence stress in metal halide perovskites. *APL Energy* **2023**, *1*, 036110.
(35) Jiang, Q.; et al. Enhanced electron extraction using SnO2 for high-efficiency planar-structure HC(NH2)2PbI3-based perovskite solar cells. *Nature Energy* **2017**, *2*, 16177.
(36) Zheng, G.; et al. Manipulation of facet orientation in hybrid perovskite polycrystalline films by cation cascade. *Nat. Commun.* **2018**, *9*, 2793.
(37) Tong, J.; et al. High-performance methylammonium-free ideal-band-gap perovskite solar cells. *Matter* **2021**, *4*, 1365−1376.
(38) Zhu, C.; et al. Strain engineering in perovskite solar cells and its impacts on carrier dynamics. *Nat. Commun.* **2019**, *10*, 815.
(39) Chen, M.; et al. Lead-Free Flexible Perovskite Solar Cells with Interfacial Native Oxide Have > 10% Efficiency and Simultaneously Enhanced Stability and Reliability. *ACS Energy Letters* **2022**, *7*, 2256−2264.
(40) Tabatabaeian, A.; et al. Residual Stress in Engineering Materials: A Review. *Adv. Eng. Mater.* **2022**, *24*, 2100786.
(41) Jiang, P.; et al. Thermal-cycle dependent residual stress within the crack-susceptible zone in thermal barrier coating system. *J. Am. Ceram. Soc.* **2018**, *101*, 4256−4261.

https://doi.org/10.1021/acsenergylett.4c00988
ACS Energy Lett. 2024, 9, 2582−2589